Available online at www.sciencedirect.com
ScienceDirect
Trans. Nonferrous Met. Soc. China 33(2023) 2406−2416
Transactions of Nonferrous Metals Society of China
www.tnmsc.cn

Transition from micro-rod to nano-lamella eutectics and its hardening effect in niobium/silicide in-situ composites

Yue-ling GUO[1,2], Si-yuan ZHANG[3], Jun-yang HE[3], Wen-jun LU[3], Li-na JIA[2], Zhi-ming LI[3], Hu ZHANG[2]

1. School of Mechanical Engineering, Beijing Institute of Technology, Beijing 100081, China;
2. Frontier Institute of Science and Technology Innovation, Beihang University, Beijing 100191, China;
3. Max-Planck-Institut für Eisenforschung, Max-Planck-Straße 1, Düsseldorf, 40237, Germany

Received 12 March 2022; accepted 14 June 2022

Abstract: To improve the mechanical properties of niobium/silicide in-situ composites via rapid solidification, the evolution of eutectic geometry and the corresponding hardening effect in a prototype Nb−18Si (at.%) composite upon electron beam surface melting (EBSM), i.e., a rapid remelting and solidifying sequence, were studied. Results show that rod-like Nb solid solution (Nbss)/Nb_3Si eutectics prevail in the arc-melted state, yet evolve into lamellar arrangements after EBSM. Atomic scale scanning transmission electron microscopy (STEM) and near-atomic scale atom probe tomography (APT) were employed to characterize the three-dimensional stacking of nano-laminated Nbss/Nb_3Si eutectics and their compositions. Compared with the rod-like eutectics, the lamellar eutectics via EBSM demonstrate a prominent eutectic refinement (39.5 nm in spacing) and an increased volume fraction of Nbss (~41%). Nano-indentation testing reveals that with the microstructural transition from micro-rod to nano-lamella eutectics, a significant increment in hardness up to 13.9 GPa is achieved.

Key words: niobium/silicide composites; rapid solidification; eutectic morphology; lamellar eutectics; rod-like eutectics

1 Introduction

Long standing needs exist for developing high-temperature structural materials in the aircraft field, which sets the pace of engine technology evolution [1]. Niobium/silicide in-situ composites, also named Nb−Si based alloys, consisting of Nb solid solution (Nbss) and silicides (Nb_3Si and/or Nb_5Si_3) have been recently developed towards advanced turbine blades, due to their relatively low densities (6.6−7.2 g/cm^3), sufficient microstructural stability and strong creep resistance at elevated temperatures, e.g., creep rates less than 3×10^{-8} s^{-1} at 1200 °C with stresses of less than 140 MPa [2−4].

One important superiority of niobium/silicide composites is the near-net shape casting ability that suits the fabrication of structure-complex components like turbine blades, including electron beam or laser additive manufacturing that is featured by a rapid solidification process [5−8]. The rules for grain nucleation and growth during additive manufacturing typically differ from conventional casting, which is considered as a near-equilibrium solidification route [4]. Therefore, it is of importance to investigate the solidification behavior of niobium/silicide composites at both near-equilibrium and non-equilibrium states, as well as the microstructural response to various solidification conditions.

Corresponding author: Yue-ling GUO, Tel: +86-10-68915087, E-mail: y.guo@bit.edu.cn;
Li-na JIA, Tel: +86-10-68916482, E-mail: jialina@buaa.edu.cn
DOI: 10.1016/S1003-6326(23)66268-5
1003-6326/© 2023 The Nonferrous Metals Society of China. Published by Elsevier Ltd & Science Press

Near-eutectic microstructures are generally engineering-favored, due to their favorable solidification behavior and attractive mechanical properties. As a typical faceted-nonfaceted system, niobium/silicide composites may display a variety of geometrical arrangements including lamellar, rod-like, dendritic and maze-like eutectics, depending on the composition, solidification conditions as well as subsequent heat treatments [9−11]. Previous work [9] has shown that the lamellar to anomalous eutectic transition can be triggered by either spark plasma sintering (SPS) or heat treatments at above 1000 °C for 1 h in rapidly solidified Nb−18Si−24Ti−2Cr−2Al (at.%) alloy powders. The anomalous eutectics refer to the irregular, broken-lamellar, and complex-regular eutectics [12]. The regular eutectics mainly include alternative rod-like and lamellar eutectics, whose regularity tends to determine their mechanical properties [13].

To tune the length scale and geometrical arrangements of eutectics for improving properties, the adjustment of composite and processing strategies are usually involved [10,11,14,15]. For instance, for directionally solidified niobium/silicide composites, both decreasing the Ti content and increasing the withdrawal rate enable the transition from quasi-regular eutectics I to quasi-regular eutectics II [10]. The former presents skewed and bifurcate morphologies with block or short-rod $(Nb, Ti)_5Si_3$, and the latter shows the paralleled growth of (Nb, Ti) solid solution phases and $(Nb, Ti)_5Si_3$ phases [10]. Fully lamellar eutectics are generated in a rapidly solidified niobium/silicide composite with a hypereutectic composition [11,16], and a further higher content of Si enables the transition from lamellar eutectics to hypereutectic dendrites [11]. Noteworthily, the transition from rod-like to lamellar eutectics, a classical microstructural response to rapid solidification [17], has not been reported for niobium/silicide composites.

In this work, we employed the electron beam surface melting (EBSM) treatment on a prototype near-eutectic Nb−18Si (at.%) composite to explore whether the rapid solidification route can effectively rebuild the eutectic morphology in terms of geometric arrangements and microstructural length-scale, as well as to reveal the potential effect on hardening behavior. To investigate the nanometer-scale microstructures, atomic scale scanning transmission electron microscopy (STEM) and near-atomic scale atom probe tomography (APT) analyses were performed for structural and chemical characterizations, respectively. Nano-indentation was conducted to evaluate the impact of tuning eutectic morphology on mechanical properties of niobium/silicide in-situ composites.

2 Experimental

A bulk Nb−18Si (at.%) composite was produced by arc-melting in argon atmosphere. The bulk ingot was remelted five times to eliminate chemical macrosegregation. An electron beam based 3D printer (Arcam A2XX), consisting of an electrical control cabinet and a vacuum chamber cabinet, was used for EBSM treatment on the arc-melted composite surface. A controlled 0.2 Pa of He was maintained in the processing chamber. A tungsten filament included in the electron gun was heated to emit electrons, which were accelerated by applying a ~60 kV voltage and focused by the electromagnetic coil. Before EBSM treatment, the bulk composite was preheated to ~1273 K using defocused electron beam to avoid cracking [16]. For EBSM treatment, focused electron beam was employed with a scanning current of 4.5 mA and a scanning speed of 700 mm/s. The zigzag scanning method was employed with a hatch distance of 0.1 mm.

Phase determination was performed by X-ray diffraction (XRD, D/max−2500, Cu K_α) at a 2θ scanning rate of 6 (°)/min. Microstructures were examined using a field-emission scanning electron microscopy (FE-SEM Merlin, Zeiss), and the attached energy dispersive X-ray spectroscopy (EDS, Esprit, Bruker) was employed for chemical measurements. Samples for the microstructure observation were ground progressively using finer grades of metallographical SiC papers, polished with diamond suspension and colloidal silica oxide polishing suspension (OPS), and finally water-cleaned to remove residual silica particles. Near-atomic-scale chemical and tomographic characterizations were performed using 3D-APT (CAMECA LEAP™ 3000X HR). APT analysis was performed using needle-shaped tips in laser pulsing mode at ~70 K with a pulse repetition of 200 kHz. The pulse energy was 0.4 nJ, and the target evaporation rate was 4 ions per 1000 pulses. The

APT data were reconstructed using CAMECA IVAS 3.8.0 software. STEM analysis was conducted on an FEI Titan Themis instrument at 300 kV. For the high angle annular dark-field (HAADF)-STEM imaging, a probe semi-convergence angle of 17 mrad was employed, and the semi-collection angles covered from 73 to 200 mrad. STEM-EDS spectrum imaging was acquired using the 4-quadrant SuperX spectrometer. Multivariate statistical analysis was applied to highlighting the signal and reducing the signal noise [18]. The site-specific TEM lamella and needle-shaped APT tips were prepared by the focused ion beam (FIB) lift-out technique (FEI Helios Nanolab 600i dual beam system). The lift-out procedure was described somewhere else [19]. A Pt layer, ~3 μm in height, was deposited on the composite surface to protect the TEM lamella from potential damage by the Ga^+ beam during the thinning process.

To evaluate the mechanical properties of the rod and lamellar eutectics, nano-indentation measurement was performed using an Agilent NanoSuite Nanoindentation G200 equipped with a Berkovich tip. The strain rate was 0.05 s^{-1}. Based on the load−displacement curve, the hardness and elastic modulus of the composite were calculated using the Oliver and Pharr's method [20].

3 Results

Figure 1 shows the XRD patterns of the arc-melted and EBSM-processed Nb−18Si composites. Both composites are composed of body-centred cubic (bcc) Nbss and tetragonal Nb_3Si phases, suggesting that the EBSM treatment does not alter the phase structures in the Nb−18Si composite.

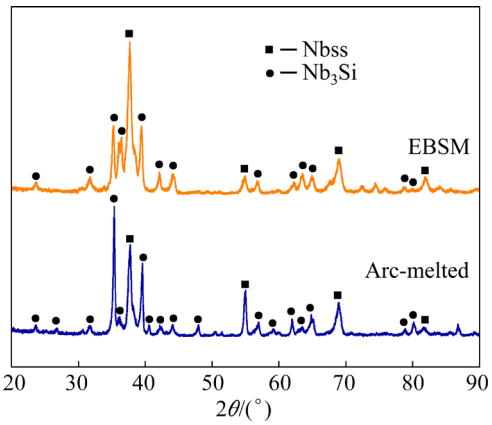

Fig. 1 XRD patterns of Nb−18Si composites processed by arc-melting and EBSM

According to the Nb−Si binary phase diagram [21], Nb_3Si is a metastable phase that typically experiences the eutectoid decomposition to Nb and Nb_5Si_3 upon equilibrium solidification. However, the decomposition of Nb_3Si is kinetically sluggish [22], resulting in the existence of undecomposed Nb_3Si after solidification. Besides, both arc-melting and EBSM deviate from equilibrium state with a more rapid solidification rate, which suppresses the decomposition of Nb_3Si, additionally contributing to the preservation of Nb_3Si phase in arc-melted and EBSM-processed Nb−18Si composites.

Backscatter-electron (BSE) imaging test was performed to observe the phase morphologies of the arc-melted Nb−18Si composite. Figure 2(a) displays

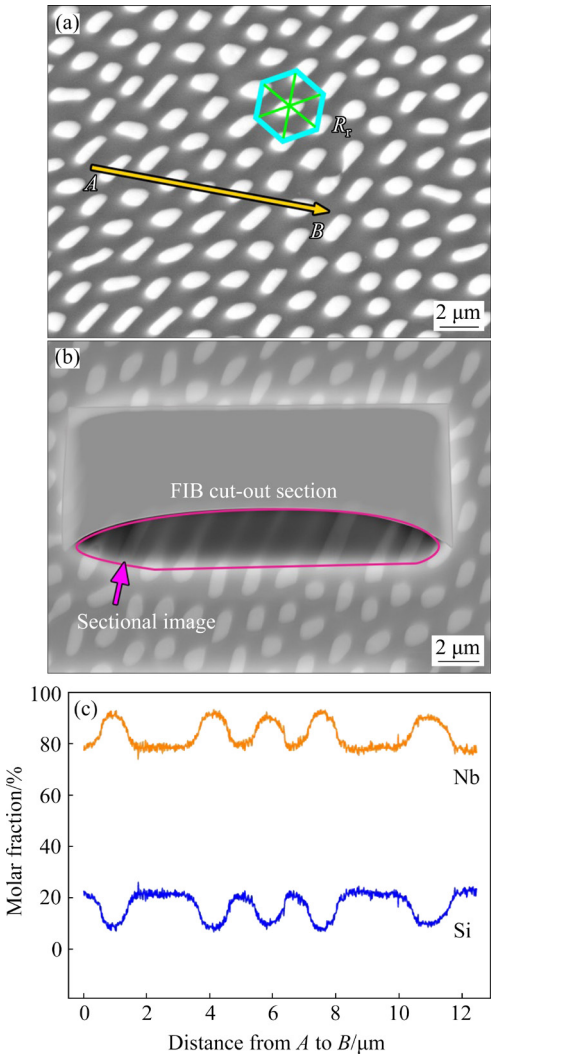

Fig. 2 Microstructure of Nb−18Si composites via arc-melting: (a) BSE image showing rod-like Nbss/Nb_3Si eutectics; (b) Sectional microstructure of rod-like eutectics; (c) Compositional distribution along line *AB* in (a)

the rod-like eutectic microstructure, and the bright-contrast Nbss rods showing a hexagonal arrangement are embedded in the dark-contrast Nb_3Si matrix. The volume fractions, approximated by the area fractions of Nbss and Nb_3Si, are (34±1)% and (66±1)%, respectively. The rod spacing (R_r), as defined in Fig. 2(a), is (1.7±0.3) μm. To further demonstrate the rod morphology of the Nbss/Nb_3Si eutectics, the FIB cut-out method was employed to observe their sectional morphology with a titling angle of 22°. As shown in Fig. 2(b), the three-dimensional rod morphology of Nbss/Nb_3Si eutectics is thus confirmed. The composition distributions of Nb and Si plotted on Fig. 2(a), are illustrated in Fig. 2(c), where both Nbss and Nb_3Si are included. The former is enriched in Nb, while the latter has a higher concentration of Si.

HAADF-STEM imaging with atomic number contrast was performed to further characterize the microstructure of Nbss/Nb_3Si eutectics formed via arc melting. Figure 3(a) shows the HAADF-STEM image of rod-like eutectics. The contents of Si in Nbss and Nb_3Si are ~8.1 and ~24.5 at.%, respectively, obtained by STEM-EDS. The fast Fourier transformation (FFT) for a sample region at the Nbss/Nb_3Si interface is displayed in Fig. 3(b), and an orientation relationship between Nbss and Nb_3Si for the arc-melted composite is found, i.e., $(110)_{Nbss}//(420)_{Nb_3Si}$ and $[001]_{Nbss}//[001]_{Nb_3Si}$. Figures 3(c) and (d) display the high-resolution HAADF-STEM images from neighboring Nb_3Si and Nbss, as overlaid with the respective crystal structures plotted using VESTA [23]. Atomic columns of Nb (red balls) in both Nb_3Si and Nbss lattices are visualized, whereas atomic columns of Si (blue balls) in Nb_3Si lattices have a very weak HAADF contrast.

The sectional microstructure of the Nb−18Si

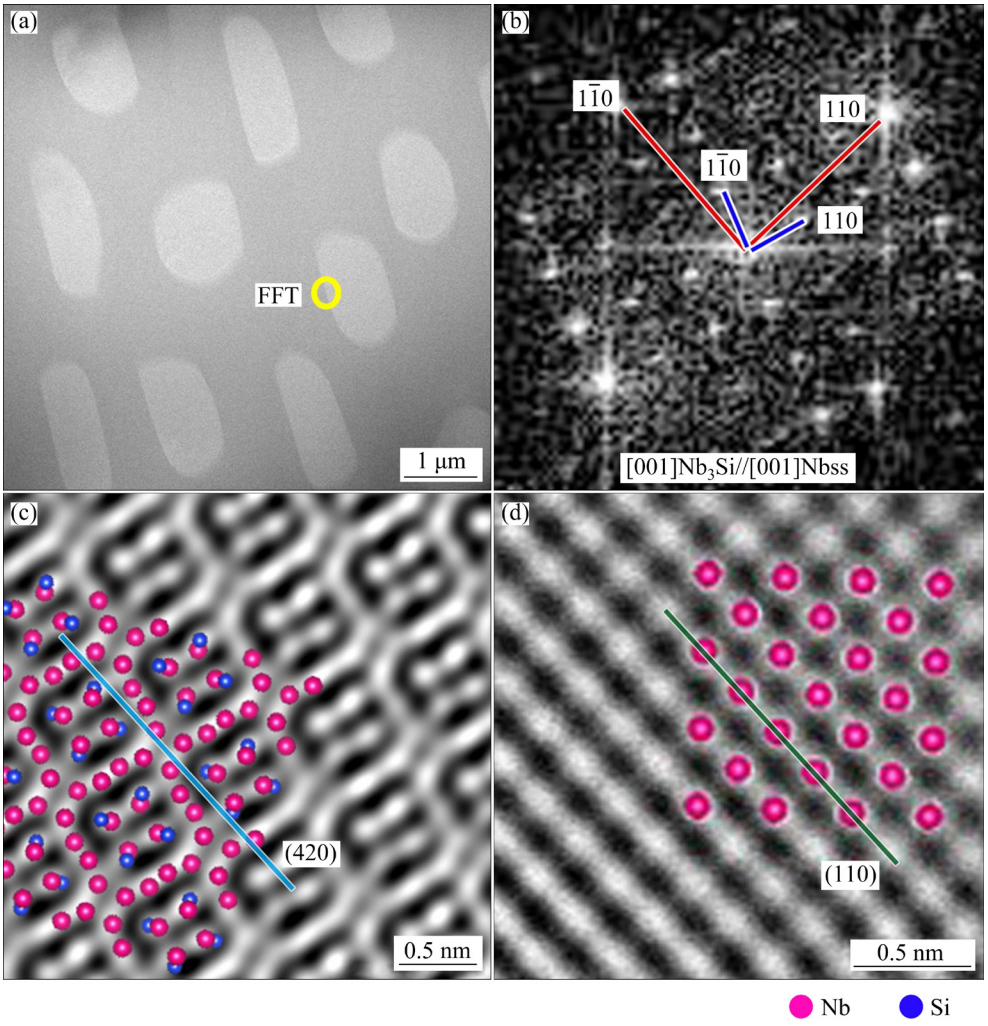

Fig. 3 HAADF-STEM image of arc-melted Nb−18Si composites (a), FFT pattern of Nbss/Nb_3Si interface (b), and high-resolution HAADF-STEM images of Nb_3Si (c) and Nbss (d), respectively, with corresponding crystal lattices generated by VESTA [23]

composite via EBSM, i.e., viewed perpendicularly to the scanning direction, is shown in Fig. 4. Accordingly, the thickness of the remelted layer via EBSM is about 73 μm. The remelted border zone is frequently observed, where Nbss particles with lighter contrast are embedded in the Nb_3Si matrix, and are featured by a coarsened microstructure (Fig. 4(b)), resulting from a lower cooling rate [16]. This observation suggests that during EBSM, the melt pool is remelted by the next electron beam scanning. In the melt pool interior, as shown in Fig. 4(c), lamellar Nbss/Nb_3Si eutectics emerge. This indicates the transition from rod-like to lamellar eutectics during EBSM.

Figure 5(a) shows the morphology of the lamellar eutectics in the EBSM-processed Nb−18Si

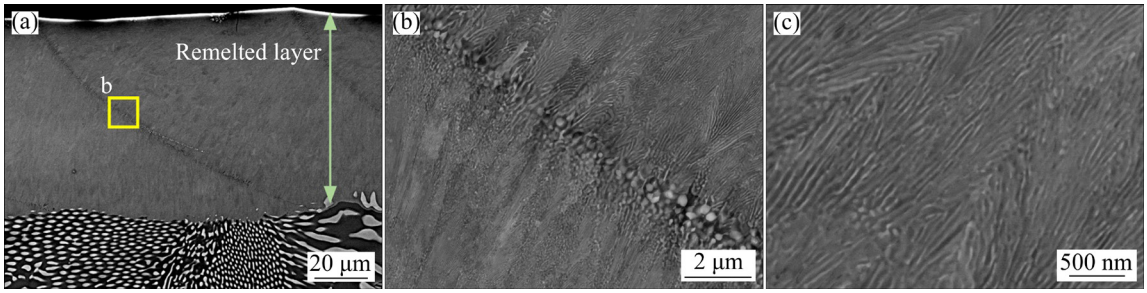

Fig. 4 Microstructure of Nb−18Si alloy via EBSM: (a) BSE image showing remelted zone; (b) Zoom-in BSE image in (a); (c) Nano-lamellar Nbss/Nb_3Si eutectics

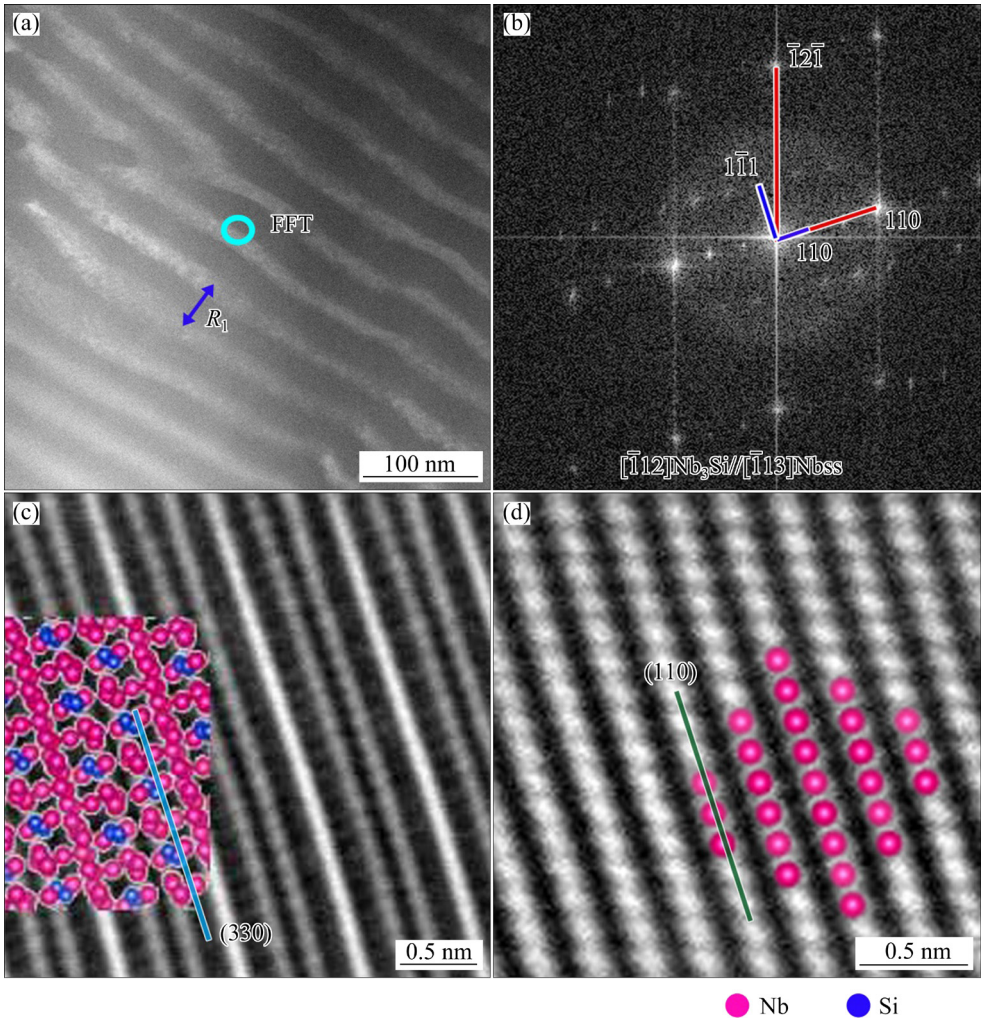

Fig. 5 HAADF-STEM image of EBSM-processed Nb−18Si composite (a), FFT pattern of Nbss/Nb_3Si interface (b), and high-magnification HAADF-STEM images of Nb_3Si (c) and Nbss (d), respectively, with crystal lattices generated by VESTA [23]

composite, via HAADF-STEM imaging. The volume fractions of Nbss and Nb_3Si, represented by area fraction estimated from multiple BSE and STEM images, are (41±2)% and (59±2)%, respectively. The lamellar spacing (R_l), defined in Fig. 5(a), is (39.5±4.8) nm, obtained from a sampling of more than 20 spacings from random locations. The fluctuation of lamellar spacing as well as the growth defects−distortion and coalescence, is revealed as a result of the variation on local solidification condition, e.g., cooling rate and temperature gradient during EBSM. The contents of Si in Nbss and Nb_3Si are ~2.1 at.% and ~27.4 at.%, respectively, as obtained by STEM-EDS. The FFT pattern of Nbss/Nb_3Si interface for the EBSM-processed composite is shown in Fig. 5(b). Accordingly, the orientation relationship between Nbss and Nb_3Si is determined as $(110)_{Nbss}//(330)_{Nb_3Si}$ and $[\bar{1}13]_{Nbss}//[\bar{1}12]_{Nb_3Si}$, which is different from that in the arc-melted composite. This orientation difference may be caused by the stronger radial temperature gradient in the melt pool produced by EBSM that tends to govern the selection of crystal orientation [24]. The atomic-resolution HAADF-STEM images from neighboring Nb_3Si and Nbss phases are shown in Figs. 5(c) and (d), respectively, correlating well with the overlaid crystal structures.

APT was utilized to unveil the elemental distribution in nanostructured Nb−18Si composite with near-atomic resolution. Figures 6(a) and (b) respectively display the reconstructed three-dimensional distribution of Nb and Si across a representative APT dataset containing both Nbss and Nb_3Si phases from the EBSM-processed composite specimen. To clearly demonstrate their lamellar morphology, the presented volume is rotated parallel to the Nbss/Nb_3Si interface in parallel with viewing direction. The distribution of Si can be used to distinguish Nbss and Nb_3Si (Fig. 6(b)). The Si-depleted region belongs to Nbss, while the Si- enriched region is Nb_3Si. The APT reconstruction containing both Nb and Si is shown in Fig. 6(c), together with an iso-composition interface of 93.0 at.% Nb. Figure 6(d) shows the representative one-dimensional compositional profiles along the selected cylinder perpendicular to the Nbss/Nb_3Si interface in Fig. 6(c). The concentrations of Si in Nbss and Nb_3Si are ~1.4 at.% and ~26.8 at.%, respectively.

To evaluate the mechanical properties of the rod and lamellar eutectics, a series of nanoindentaion tests were performed, as shown in Fig. 7. The representative load−displacement responses for the two types of eutectics are illustrated in Fig. 7(a) with a maximum load of 670 mN. The hardness of the lamellar eutectics via EBSM is (13.9±0.7) GPa, ~20% higher than that of the rod eutectics via arc

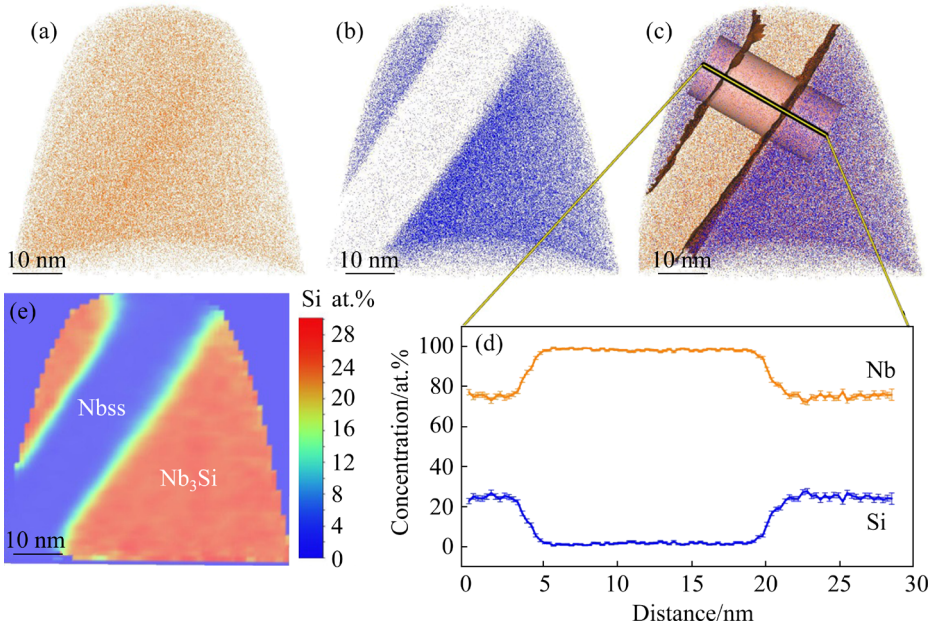

Fig. 6 APT analysis of lamellar Nbss/Nb_3Si eutectics: (a, b) Distribution of Nb and Si, respectively; (c) Reconstruction of dataset with iso-composition interface at 93.0 at.% Nb; (d) One-dimensional compositional profile along cylinder denoted in (c); (e) 2D compositional map

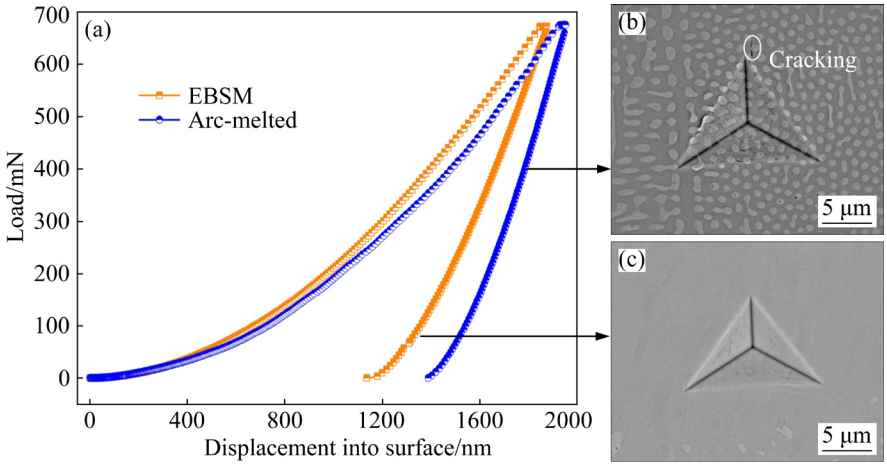

Fig. 7 Representative load−displacement curves obtained from nano-indentation on arc-melted and EBSM-processed Nb−18Si composites (a), and morphologies of indentation impress on arc-melted (b) and EBSM-processed (c) alloys, respectively

melting ((11.6±0.6) GPa). The elastic modulus of the lamellar eutectics via EBSM is (191.9±6.8) GPa, slightly lower than that of the rod eutectics via arc-melting ((209.7±4.1) GPa). It is also noted that cracking occurs at the indentation impress corners, which may indicate a lower fracture toughness of the rod eutectics (Fig. 7(b)) [16,25]. Therefore, when comparing the mechanical performance of the rod-like and lamellar eutectics, we find that the lamellar eutectics show higher resistance to localized plastic deformation (hardness), and lower resistance to elastic deformation (elastic modulus).

4 Discussion

4.1 Rod-like to lamellar eutectics transition

Rod and lamella are two most important morphologies of eutectics. The rod to lamellar eutectics transition, a fundamental subject in solidification theory, has been observed in other systems including Al−Cu [26], Al−Fe [27], Ni−Al [28], Mg−Li [29] alloys. For the first time, we not only achieve such microstructural transition in niobium/silicide composite family but also reduce the eutectic spacing from >1 μm down to <50 nm, as schematically illustrated in Fig. 8. The classical model for the selection of either rod-like or lamellar eutectics is based on the competitive growth criteria such that the growth morphology with higher solidification temperature (lower undercooling) will prevail [30−32]. The resulted microstructure transition condition depends on the volume fraction of the minor phase and the relative interface energy contribution. In practice, this transition is not sharp but happens in a small range [32]. Accordingly, rod-like eutectics are generally stable when the volume fraction of the minor phase is lower than $1/\pi$, assuming isotropic interfacial energy, and transformed into the lamellar morphology with a higher volume fraction [30]. Here, in our case, for the experimental Nb−18Si composites, the volume fraction of Nbss in rod-like eutectics is ~34%, close to $1/\pi$. In contrast, the volume fraction of Nbss in lamellar eutectics via EBSM with refined eutectic spacings is ~41%, much higher than $1/\pi$. This supports the idea that the volume fraction change of Nbss is the key factor behind this transition mediated by the EBSM treatment.

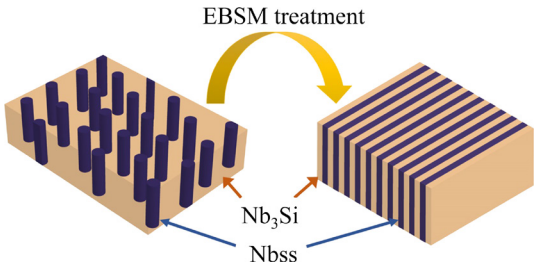

Fig. 8 Schematic of microstructural transition from rod to lamellar eutectics triggered by EBSM treatment

In addition, other effects such as the orientation relationship between two phases can also play a role in the microstructural transition. The classical theory often assumes that the interfacial free energy is isotropic, so the orientation

does not matter [32]. This simplification, often made for building analytical models, is not always true. Our experiments (Figs. 3 and 5) reveal that the orientation between two phases follow specific relationships, and clear evidence that the interfacial free energy is not isotropic. Another evidence is that the regularity of eutectic rods in Fig. 2 is not perfect, which is only possible for isotropic interfacial energy [33,34]. It is expected that this effect may shift the critical volume fraction for the rod-like to lamellar eutectics transition. Taking the anisotropy in the interfacial free energy into account would require a more detail model development. But in both cases (with or without anisotropy), the volume fraction of Nbss phase remains to be the most important aspect, which also apply to our niobium/silicide composites' results in this work.

Since the volume fractions of the two phases are the key factor determining the rod-like to lamellar eutectics transition, now the question becomes why the volume factions are changed upon EBSM processing. The volume fractions depend on the molar fractions of the two phases and their molar volumes, which both depend on temperature and composition. On the one hand, the change of lattice constant (molar fraction) with composition, also known as the Vegard's coefficient [35], is often small, so is the thermal expansion coefficient. Therefore, the molar volume effect is negligible. On the other hand, according to the lever rule [36], the molar fractions are determined by the compositions of the two phases for a fixed nominal composition. As confirmed by our results, although the phase structures are the same, their compositions do change from one process to another (arc-melting vs EBSM) due to the difference in solidification conditions. It is worth noting that the Si content in Nb_3Si in the EBSM-processed composite is higher than that in the arc-melted composite, as verified by STEM-EDS and APT measurements. Meanwhile, the Si content in Nbss shows the opposite trend. Such a change on the Si content can be related to the energetic effects of site-ordering [37,38]. As a consequence, higher volume fraction of Nbss is formed in the EBSM-processed composite to partition the 18 at.% Si with Nb_3Si, leading to the formation of a lamellar microstructure.

In addition, rod-like to lamellar eutectics transition can be understood from stability analysis considering the capillary effect, namely the Rayleigh instability [26,39,40], as documented in a recent model developed by LIU et al [26]. For a stationary cylinder with fixed volume, it has been well established that the cylinder will remain stable in the longitudinal direction with perturbation wavelength $\lambda_z<2\pi R$, where R is the radius of the unperturbed cylinder [26,39]. The eutectic spacing (~39.5 nm) is significantly smaller than that of the rod spacing (~1.7 μm). With such a eutectic spacing increment, the eutectic lamellae tend to be unstable and divide into rods, resulting in the formation of rod-like eutectics.

Accompanied with the microstructural transition, significant microstructural refinement is realized, arising from the rapid solidification condition enabled by EBSM. Owing to the substantial high energy density of the electron beam, higher temperature gradient (G) and larger growth velocity (V) are achieved by EBSM, compared with arc melting. Resultantly, the cooling rate (product of G and V) by EBSM (10^3−10^5 K/s) is much higher than that by arc melting (<10^2 K/s) [41,42]. The coupled diffusion field distance required for the growth of Nbss/Nb_3Si eutectics via EBSM thus substantially decreases, resulting in the nanoscale microstructure.

4.2 Hardening mediated by microstructural transition

For Nbss/Nb_3Si composite consisting of a soft metal phase and a hard intermetallic phase, the composite's hardness is mainly determined by the eutectic morphology, volume fraction of each phase and the number of boundaries. It has been reported that the lamellar eutectic morphology enables a more favorable combination of strength and plasticity, while the rod-like arrangement generates a higher strength at the expense of plasticity, being less effective in managing local deformation instabilities [43]. Meanwhile, combining with the rationale that the hardness of Nb_3Si is much higher than that of Nbss [44], the rod-like eutectics with a higher fraction of Nb_3Si should have shown a higher hardness value than the lamellar eutectics from the above two viewpoints. However, our experimental results show the opposite trend, providing an even higher hardness for the lamellar eutectics. This hardness increment arising from the microstructural transition from rod to lamellar eutectics is mainly associated with the significant

microstructure refinement of the nano-lamellar eutectics, producing more boundaries to impede dislocation movement. The concept of laminated nano-composites has been introduced in various materials systems, e.g., Cu/Zr, Cu/Nb, and Ag/Ni, and demonstrated to improve both the strength and the ductility [45,46]. The nano-lamellar eutectic niobium/silicide composites via EBSM have also shown the improvement in mechanical properties. Such a rationale can be further engineered by electron beam additive manufacturing to fabricate niobium/silicide composite components, with the additional consideration on the effects of thermal history during additive manufacturing on the microstructure and mechanical properties [47].

5 Conclusions

(1) Rod-like Nbss/Nb_3Si eutectics are formed in the Nb−18Si composite via arc-melting, and the Nbss rods, embedded in the Nb_3Si matrix, show a hexagonal geometric arrangement.

(2) The transition from rod-like to lamellar eutectics is triggered by the EBSM treatment while maintaining the Nbss/Nb_3Si phase regime. The volume fraction of Nbss in lamellar eutectics via EBSM ((41±2)%) is higher than that in rod-like eutectics via arc-melting ((34±1)%).

(3) Accompanied with this microstructural transition, significant microstructure refinement is achieved, resulting in the formation of alternating Nbss and Nb_3Si lamellae with a spacing of ~39.5 nm. Compared with the rod-like eutectics, the lamellar eutectics show an increased hardness ((13.9±0.7) GPa) and a slightly decreased elastic modulus ((191.9±6.8) GPa).

(4) The results provide new microstructural insights towards the electron beam melting of niobium/silicide composites with improved mechanical properties.

Acknowledgments

The authors gratefully acknowledge the financial support from China Postdoctoral Science Foundation (No. 2021M690384), and the National Natural Science Foundation of China (No. 51571004). The authors would like to acknowledge Dr. Hui PENG at Beihang University for performing the EBSM treatment. The authors also would like to acknowledge the kind support of M. NELLESSEN, U. TEZINS and A. STURM at the Max-Planck-Institut für Eisenforschung for the experimental training.

References

[1] POLLOCK T M. Alloy design for aircraft engines [J]. Nature Materials, 2016, 15(8): 809−815.

[2] BEWLAY B P, JACKSON M R, SUBRAMANIAN P R, ZHAO J C. A review of very-high-temperature Nb-silicide-based composites [J]. Metallurgical and Materials Transactions A, 2003, 34(10): 2043−2052.

[3] ZHANG S N, JIA L N, GUO Y L, KONG B, ZHOU C G, ZHANG H. Improvement in the oxidation resistance of Nb−Si−Ti based alloys containing zirconium [J]. Corrosion Science, 2020, 163: 108294.

[4] QIAO Y Q, GUO X P, ZENG Y X. Study of the effects of Zr addition on the microstructure and properties of Nb−Ti−Si based ultrahigh temperature alloys [J]. Intermetallics, 2017, 88: 19−27.

[5] FÖRNER A, VOLLHÜTER J, HAUSMANN D, ARNOLD C, FELFER P, NEUMEIER S, GÖKEN M. Nanostructuring of Nb−Si−Cr alloys by electron beam melting to improve the mechanical properties and the oxidation behavior [J]. Metallurgical and Materials Transactions A, 2021, 53(1): 240−249.

[6] WANG P, GOH M H, LI Q, NAI M L S, WEI J. Effect of defects and specimen size with rectangular cross-section on the tensile properties of additively manufactured components [J]. Virtual and Physical Prototyping, 2020, 15(3): 251−264.

[7] ZHAI W G, WANG P, NG F L, ZHOU W, NAI S M L, WEI J. Hybrid manufacturing of γ-TiAl and Ti−6Al−4V bimetal component with enhanced strength using electron beam melting [J]. Composites Part B: Engineering, 2021, 207: 108587.

[8] LIU T Y, MIN X H, ZHANG S, WANG C S, DONG C. Microstructures and mechanical properties of Ti−Al−V−Nb alloys with cluster formula manufactured by laser additive manufacturing [J]. Transactions of Nonferrous Metals Society of China, 2021, 31(10): 3012−3023.

[9] GUO Y L, JIA L N, KONG B, ZHANG S N, SHA J B, ZHANG H. Microstructure transition from lamellar eutectic to anomalous eutectic of Nb−Si based alloy powders by heat treatment and spark plasma sintering [J]. Journal of Alloys and Compounds, 2017, 696: 516−521.

[10] WANG N, JIA L N, KONG B, GUO Y L, ZHANG H R, ZHANG H. Eutectic evolution of directionally solidified Nb−Si based ultrahigh temperature alloys [J]. International Journal of Refractory Metals and Hard Materials, 2018, 71(Supplement C): 273−279.

[11] GUO Y L, JIA L N, HE J Y, ZHANG S Y, LI Z M, ZHANG H. Interplay between eutectic and dendritic growths dominated by Si content for Nb−Si−Ti alloys via rapid solidification [J]. Journal of Manufacturing Science and Engineering, 2022, 144: 061007.

[12] CROKER M N, BARAGAR D, SMITH R W. Anomalous eutectic growth: II. The relationship between faceted/non-faceted eutectic structures [J]. Journal of Crystal Growth,

1975, 30(2): 198−212.

[13] DORCHEH A S, DONNER W, GALETZ M C. From eutectic to peritectic: Effect of Ge on morphology, structure, and coarsening of Cr−Cr_3Si alloys [J]. Intermetallics, 2018, 93: 201−208.

[14] GUO H S, GUO X P. Microstructure evolution and room temperature fracture toughness of an integrally directionally solidified Nb−Ti−Si based ultrahigh temperature alloy [J]. Scripta Materialia, 2011, 64(7): 637−640.

[15] LIU W, XIONG H P, LI N, GUO S Q, QIN R Y. Microstructure characteristics and mechanical properties of Nb−17Si−23Ti ternary alloys fabricated by in situ reaction laser melting deposition [J]. Acta Metallurgica Sinica (English Letters), 2018, 31(4): 362−370.

[16] GUO Y L, LIANG Y J, LU W J, JIA L N, LI Z M, PENG H, ZHANG H. Competitive growth of nano-lamellae Nb/Nb_3Si eutectics with enhanced hardness and toughness[J]. Applied Surface Science, 2019, 486: 22−27.

[17] TRIVEDI R, WANG N. Theory of rod eutectic growth under far-from-equilibrium conditions: Nanoscale spacing and transition to glass [J]. Acta Materialia, 2012, 60(6/7): 3140−3152.

[18] ZHANG S Y, SCHEU C. Evaluation of EELS spectrum imaging data by spectral components and factors from multivariate analysis [J]. Microscopy, 2018, 67: i133−i141.

[19] THOMPSON K, LAWRENCE D, LARSON D J, OLSON J D, KELLY T F, GORMAN B. In situ site-specific specimen preparation for atom probe tomography [J]. Ultramicroscopy, 2007, 107(2/3): 131−139.

[20] OLIVER W C, PHARR G M. An improved technique for determining hardness and elastic modulus using load and displacement sensing indentation experiments [J]. Journal of Materials Research, 1992, 7(6): 1564−1583.

[21] SCHLESINGER M E, OKAMOTO H, GOKHALE A B, ABBASCHIAN R. The Nb−Si (niobium−silicon) system [J]. Journal of Phase Equilibria, 1993, 14(4): 502−509.

[22] AMANCHERLA S, KAR S, BEWLAY B, YING Y, CHANG A. Thermodynamic and microstructural modeling of Nb−Si based alloys [J]. Journal of Phase Equilibria and Diffusion, 2007, 28(1): 2−8.

[23] MOMMA K, IZUMI F. VESTA 3 for three-dimensional visualization of crystal, volumetric and morphology data [J]. Journal of Applied Crystallography, 2011, 44(6): 1272−1276.

[24] LIANG Y J, CHENG X, WANG H M. A new microsegregation model for rapid solidification multicomponent alloys and its application to single-crystal nickel-base superalloys of laser rapid directional solidification [J]. Acta Materialia, 2016, 118: 17−27.

[25] MAKUCH N. Influence of nickel silicides presence on hardness, elastic modulus and fracture toughness of gas-borided layer produced on Nisil-alloy [J]. Transactions of Nonferrous Metals Society of China, 2021, 31(3): 764−778.

[26] LIU S, LEE J H, TRIVEDI R. Dynamic effects in the lamellar–rod eutectic transition [J]. Acta Materialia, 2011, 59(8): 3102−3115.

[27] HUGHES I R, JONES H. Coupled eutectic growth in Al−Fe alloys [J]. Journal of Materials Science, 1976, 11(10): 1781−1793.

[28] QUE Z P, GU J H, SHIN J H, CHOI H K, JUNG Y G, LEE J H. Lamellar to rod eutectic transition in the hypereutectic nickel-aluminum alloy [J]. Materials Today: Proceedings, 2014, 1(1): 17−24.

[29] LIU D, ZHANG H W, LI Y X, CHEN X, LIU Y. Effects of composition and growth rate on the microstructure transformation of β-rods/lamellae/α-rods in directionally solidified Mg−Li alloy [J]. Materials & Design, 2017, 119: 199−207.

[30] JACKSON K A, HUNT J D. Lamellar and rod eutectic growth [M]. Amsterdam: Elsevier, 1988: 363−376.

[31] LIN X, CAO Y Q, WANG Z T, CAO J, WANG L L, HUANG W D. Regular eutectic and anomalous eutectic growth behavior in laser remelting of Ni−30wt.%Sn alloys [J]. Acta Materialia, 2017, 126: 210−220.

[32] TRIVEDI R, MAGNIN P, KURZ W. Theory of eutectic growth under rapid solidification conditions [J]. Acta Metallurgica, 1987, 35(4): 971−980.

[33] JIANG M, HU X, LI J, WANG Z, WANG J. An interface-oriented data-driven scheme applying into eutectic patterns evolution [J]. Materials & Design, 2022, 223: 111222.

[34] KHANNA S, ARAMANDA S K, CHOUDHURY A. Role of solid–solid interfacial energy anisotropy in the formation of broken lamellar structures in eutectic systems [J]. Metallurgical and Materials Transactions A, 2020, 51(12): 6327−6345.

[35] DENTON A R, ASHCROFT N W. Vegard's law [J]. Physical Review A, 1991, 43(6): 3161−3164.

[36] TAVAKOLI R. Smooth modeling of solidification based on the latent heat evolution approach [J]. The International Journal of Advanced Manufacturing Technology, 2017, 88(9/10/11/12): 3041−3052.

[37] ASSADI H, GREER A L. Site-ordering effects on element partitioning during rapid solidification of alloys [J]. Nature, 1996, 383(6596): 150−152.

[38] ZHANG J B, WANG H E, KUANG W W, ZHANG Y C, LI S, ZHAO Y H, HERLACH D M. Rapid solidification of non-stoichiometric intermetallic compounds: Modeling and experimental verification [J]. Acta Materialia, 2018, 148: 86−99.

[39] JIANG Z Y, JIANG Q R, HUANG R, SUN M J, WANG K L, KUANG Q, ZHU Z Z, XIE Z X. Chemically initiated liquid-like behavior and fabrication of periodic wavy Cu/CuAu nanocables with enhanced catalytic properties [J]. Nanoscale, 2018, 10(19): 9012−9020.

[40] CHANDA B, PANI S K, DAS J. Mechanism of microstructure evolution and spheroidization in ultrafine lamellar CoCrFeNi($Ni_{0.5}$/$Ta_{0.4}$) eutectic high entropy alloys upon hot deformation [J]. Materials Science and Engineering: A, 2022, 835: 142669.

[41] AL-BERMANI S S, BLACKMORE M L, ZHANG W, TODD I. The origin of microstructural diversity, texture, and mechanical properties in electron beam melted Ti−6Al−4V [J]. Metallurgical and Materials Transactions A, 2010, 41(13): 3422−3434.

[42] DAS J, TANG M B, KIM K B, THEISSMANN R, BAIER F, WANG W H, ECKERT J. "Work-hardenable" ductile bulk metallic glass [J]. Physical Review Letters, 2005, 94(20):

205501.
[43] AZADEHRANJBAR S, WEI B Q, XIE D Y, MING K S, WANG J, SHIELD J E. Strength and plasticity of lamellar vs. fibrous eutectic Mg−Al nanocomposites: An in-situ micro-compression study [J]. Acta Materialia, 2021, 206: 116624.
[44] GUO E Y, SINGH S S, MAYER C, MENG X Y, XU Y J, LUO L S, WANG M, CHAWLA N. Effect of gallium addition on the microstructure and micromechanical properties of constituents in NbSi based alloys [J]. Journal of Alloys and Compounds, 2017, 704: 89−100.
[45] LI J J, LU W J, GIBSON J, ZHANG S Y, KORTE-KERZEL S, RAABE D. Compatible deformation and extra strengthening by heterogeneous nanolayer composites [J]. Scripta Materialia, 2020, 179: 30−35.
[46] NASIM M, LI Y C, WEN M, WEN C E. A review of high-strength nanolaminates and evaluation of their properties [J]. Journal of Materials Science & Technology, 2020, 50: 215−244.
[47] CAGIRICI M, WANG P, NG F L, NAI M L S, DING J, WEI J. Additive manufacturing of high-entropy alloys by thermophysical calculations and in situ alloying [J]. Journal of Materials Science & Technology, 2021, 94: 53−66.

铌/硅化物原位自生复合材料微米棒状向纳米层片状共晶组织转变及其硬化行为

郭跃岭[1,2]，张思源[3]，何骏阳[3]，逯文君[3]，贾丽娜[2]，李志明[3]，张 虎[2]

1. 北京理工大学 机械与车辆学院，北京 100081；
2. 北京航空航天大学 前沿科学技术创新研究院，北京 100191；
3. Max-Planck-Institut für Eisenforschung, Max-Planck-Straße 1, Düsseldorf, 40237, Germany

摘 要：以 Nb−18Si(摩尔分数，%)复合材料为研究对象，分析共晶组织几何形态对电子束表面熔化(EBSM)快速凝固条件的响应机理及其对材料硬度的影响规律。研究结果表明，Nbss/Nb_3Si 共晶在电弧熔炼凝固条件下以棒状形态为主，而在 EBSM 凝固条件下转变为层片状形态。利用原子尺度的扫描透射电子显微镜(STEM)和近原子尺度的三维原子探针(APT)对样品进行表征，获得纳米 Nbss/Nb_3Si 共晶的三维层片状结构特征及其组分。与棒状共晶相比，EBSM 凝固条件下形成的层片状共晶组织显著细化(共晶间距为 39.5 nm)，Nbss 相体积分数大幅增加(约 41%)。随着显微组织由微米棒状共晶转变为纳米层片状共晶，材料硬度显著增加，达到 13.9 GPa。

关键词：铌/硅化物复合材料；快速凝固；共晶形态；层片状共晶；棒状共晶

(Edited by Xiang-qun LI)